Uniaxial strain control of spin-polarization in multicomponent nematic order of $BaFe_2As_2$

T. Kissikov,[1] R. Sarkar,[2] M. Lawson,[1] B. T. Bush,[1] E. I. Timmons,[3] M. A. Tanatar,[3]
R. Prozorov,[3] S. L. Bud'ko,[3] P. C. Canfield,[3] R. M. Fernandes,[4] and N. J. Curro[1]

[1]*Department of Physics, University of California, Davis, California 95616, USA*
[2]*Institute for Solid State Physics, TU Dresden, D-01069 Dresden, Germany*
[3]*Ames Laboratory U.S. DOE and Department of Physics and Astronomy,Iowa State University, Ames, Iowa 50011, USA*
[4]*School of Physics and Astronomy, University of Minnesota, Minneapolis, Minnesota 55455, USA*

(Dated: April 13, 2017)

The iron-based high temperature superconductors exhibit a rich phase diagram reflecting a complex interplay between spin, lattice, and orbital degrees of freedom [1–4]. The nematic state observed in many of these compounds epitomizes this complexity, by entangling a real-space anisotropy in the spin fluctuation spectrum with ferro-orbital order and an orthorhombic lattice distortion [5–7]. A more subtle and much less explored facet of the interplay between these degrees of freedom arises from the sizable spin-orbit coupling present in these systems, which translates anisotropies in real space into anisotropies in spin space. Here, we present a new technique enabling nuclear magnetic resonance under precise tunable strain control, which reveals that upon application of a tetragonal symmetry-breaking strain field, the magnetic fluctuation spectrum in the paramagnetic phase of $BaFe_2As_2$ also acquires an anisotropic response in spin-space. Our results unveil a hitherto uncharted internal spin structure of the nematic order parameter, indicating that similar to liquid crystals, electronic nematic materials may offer a novel route to magneto-mechanical control.

In the absence of external strain, $BaFe_2As_2$ undergoes a weakly first-order antiferromagnetic phase transition at $T_N = 135$K, accompanied by an orthorhombic structural distortion that breaks the tetragonal symmetry of the unit cell in the paramagnetic phase. The relatively small orthorhombic lattice distortion ($\sim 0.3\%$) [5] is driven by a nematic instability [8], whose electronic origin is manifested by the large in-plane resistivity anisotropy ($\sim 100\%$) [9, 10]. Despite being simultaneous in $BaFe_2As_2$, the nematic and antiferromagnetic transition temperatures, T_s and T_N, split upon doping, giving rise to a regime with long-range nematic order but no antiferromagnetic order, since $T_N < T_s$ [1, 11].

The close relationship between nematicity and the magnetic degrees of freedom can be seen directly from the stripe-like nature of the antiferromagnetic state, which orders with one of two possible wave-vectors related by a 90° rotation: $\mathbf{Q}_1 = (\pi, 0)$ (corresponding to spins parallel along the y axis and anti-parallel along x) and $\mathbf{Q}_2 = (0, \pi)$ (corresponding to spins parallel along x and anti-parallel along y). Below T_N nearest neighbor spins are parallel or antiparallel depending on whether they are connected by a short or long bond, however above T_N but below T_s the magnetic fluctuations centered around $\mathbf{Q}_1$ become weaker or stronger than those centered around $\mathbf{Q}_2$, depending on whether the b axis is parallel or perpendicular to $\mathbf{Q}_1$, respectively. Mathematically, this allows one to define the nematic order parameter $\bar{\varphi}$ in terms of the (spin unpolarized) magnetic susceptibility $\chi(\mathbf{q})$ according to $\bar{\varphi} \equiv \chi^{-1}(\mathbf{Q}_2) - \chi^{-1}(\mathbf{Q}_1)$ [2]. Such an interplay between nematic and spin degrees of freedom has been indeed observed by neutron scattering [6, 7, 12, 13] and nuclear magnetic resonance (NMR) [14–16] experiments in detwinned $BaFe_2As_2$ crystals.

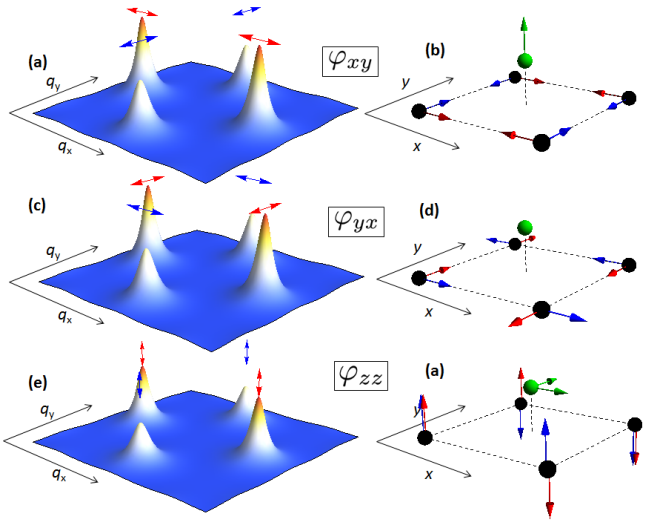

FIG. 1. Spin fluctuations in momentum space (left) and in real space (right) and polarization directions of the Fe spins for the three nematic components, φ_{xy} (a,b), φ_{yx} (c,d), and φ_{zz} (e,f). The red arrows correspond to the magnetic ordering vector $\mathbf{Q}_1 = (\pi, 0)$ and the blue arrows correspond to $\mathbf{Q}_2 = (0, \pi)$. The black spheres are the Fe sites, the green sphere is the As site, and the green arrows indicate the direction of the hyperfine field.

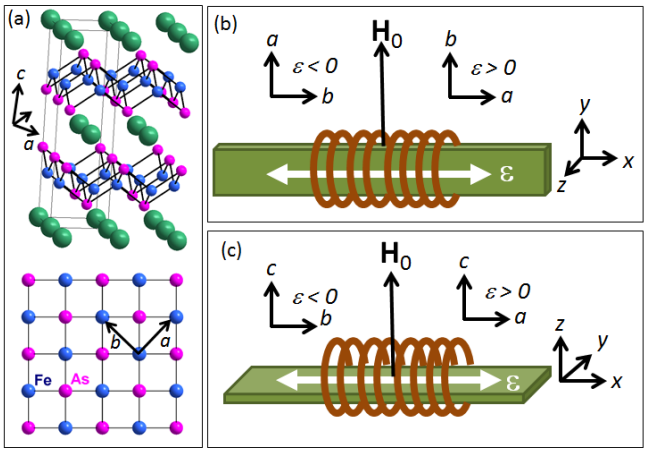

FIG. 2. (a) Crystal structure of $BaFe_2As_2$, with Ba (green), Fe (blue) and As (magenta) sites shown. Lower panel shows the Fe-As plane in the tetragonal phase, with arrows indicating the unit cell axes of the orthorhombic phase ($\mathbf{a} \parallel (110)_{tet}$, $\mathbf{b} \parallel (1\bar{1}0)_{tet}$). (b,c) Orientation of the magnetic field with respect to the coil (H_1) and strain axis for $\mathbf{H}_0 \perp \mathbf{c}$ (b) and $\mathbf{H}_0 \parallel \mathbf{c}$ (c). For positive (tensile) strain $\mathbf{H}_0$ is parallel to $\mathbf{b}$, whereas for negative (compressive) strain $\mathbf{H}_0$ is along $\mathbf{a}$.

However, orbital degrees of freedom also participate actively in the nematic phase. This leads to the well known effect that tetragonal symmetry-breaking is also manifested by a ferro-orbital polarization that makes the occupation of the Fe d_{xz} orbitals different than the occupation of the Fe d_{yz} orbitals. A less explored effect emerges from the relatively sizable spin-orbit coupling (SOC), which converts anisotropies in real space into anisotropies in spin space. On one hand, SOC enforces the spins to point along the ordering vector direction below T_N. On the other hand, SOC leads to different magnitudes of the diagonal spin susceptibility components, $\chi_{\alpha\alpha}(\mathbf{q})$ with $\alpha = (x, y, z)$, in the nematic temperature regime, $T_N < T < T_s$. As a result, the nematic order parameter naturally acquires an internal spin structure, since generically one must define $\varphi_{\alpha\beta} = \chi^{-1}_{\alpha\alpha}(\mathbf{Q}_2) - \chi^{-1}_{\beta\beta}(\mathbf{Q}_1)$. Clearly, the nematic order parameter $\bar{\varphi}$ defined above can be understood as an average over all possible polarizations, $\bar{\varphi} = \frac{1}{9}\sum_{\alpha\beta}\varphi_{\alpha\beta}$. The space-group symmetry of the iron pnictides enforces many of these combinations to vanish, yielding only three non-zero independent components: φ_{xy}, φ_{yx}, and φ_{zz}. The physical meaning of each component is depicted in Fig. 1; for instance, φ_{xy} is a measure of the asymmetry between spin fluctuations peaked at $\mathbf{Q}_1$ and polarized along the x axis, and spin fluctuations peaked at $\mathbf{Q}_2$ and polarized along the y axis.

Elucidating the hitherto unkown spin structure of the nematic order parameter is fundamental to shed light on the intricate interplay between orbital, spin, and lattice degrees of freedom, which are ultimately responsible for the superconducting instability of the system. In this paper, we perform NMR spin-lattice relaxation measurements to probe the anisotropy of the spin fluctuations under fixed strain in the paramagnetic phase of $BaFe_2As_2$. The role of the applied uniaxial strain is to provide a small tetragonal symmetry-breaking field, akin to externally applied magnetic fields in ferromagnets. In contrast to previous works, here we probe the magnetic fluctuations anisotropy both in real space and in spin space – more specifically, we determine each of the nematic susceptibilities associated with the three nematic components φ_{xy}, φ_{yx}, and φ_{zz}. This is possible because the magnetic fluctuations associated with each spin polarization pattern generate very different types of fluctuating local fields experienced by the ^{75}As nuclear spin ($I = 3/2$), which couples to the four nearest neighbor Fe spins via a transferred hyperfine interaction (see Fig. 1) [17]. Our main result is that the three nematic components respond differently to external strain, i.e. nematic order induces not only real-space anisotropy, but also affects the spin-space anisotropy. In particular, we find that the out-of-plane spin fluctuations centered at $\mathbf{Q} \parallel \hat{a}$ are more strongly enhanced by the strain, as compared to the spin fluctuations polarized along the longer in-plane axis. This raises the interesting possibility of reversing the spin polarization of the system from in-plane to out-of-plane by applying a sufficiently strong in-plane strain. More broadly, our results thus opens a new avenue toward magneto-mechanical manipulation of strongly correlated systems that display nematic order.

Key to this study is our ability to control precisely the uniaxial strain applied in the sample, which is achieved by integrating a novel piezoelectric strain cell with an NMR probe. This new device is based upon a design used previously to investigate the superconducting transition temperature of Sr_2RuO_4 [18, 19], and can achieve both positive and negative strains with large strain homogeneity. This device differs from the horseshoe-clamp [9] used previously for NMR [15], and offers superior control over the sample alignment and the level of strain applied.

Single crystals of $BaFe_2As_2$ were cut along the tetragonal (110) direction and mounted in the cryogenic strain cell with field oriented both parallel and perpendicular to the crystallographic c-axis, as shown in Fig. 2. The strain cell contains two sets of piezoelectric stacks, one inner and two outer. Because the sample is freely suspended between the piezoelectric stacks rather than glued down over a portion of the stack, the full displacement of each stack is transferred to the sample. As a result the device is able to achieve displacements of $\pm 6\mu$m at room temperature and $\pm 3\mu$m at 4K, corresponding to strains of the order of 10^{-3} in this material. A free-standing NMR coil was placed around the sample prior to securing the ends of the crystal in the strain device with epoxy. The radiofrequency field $\mathbf{H}_1$ is oriented parallel to the strain axis, which is always perpendicular to the external field,

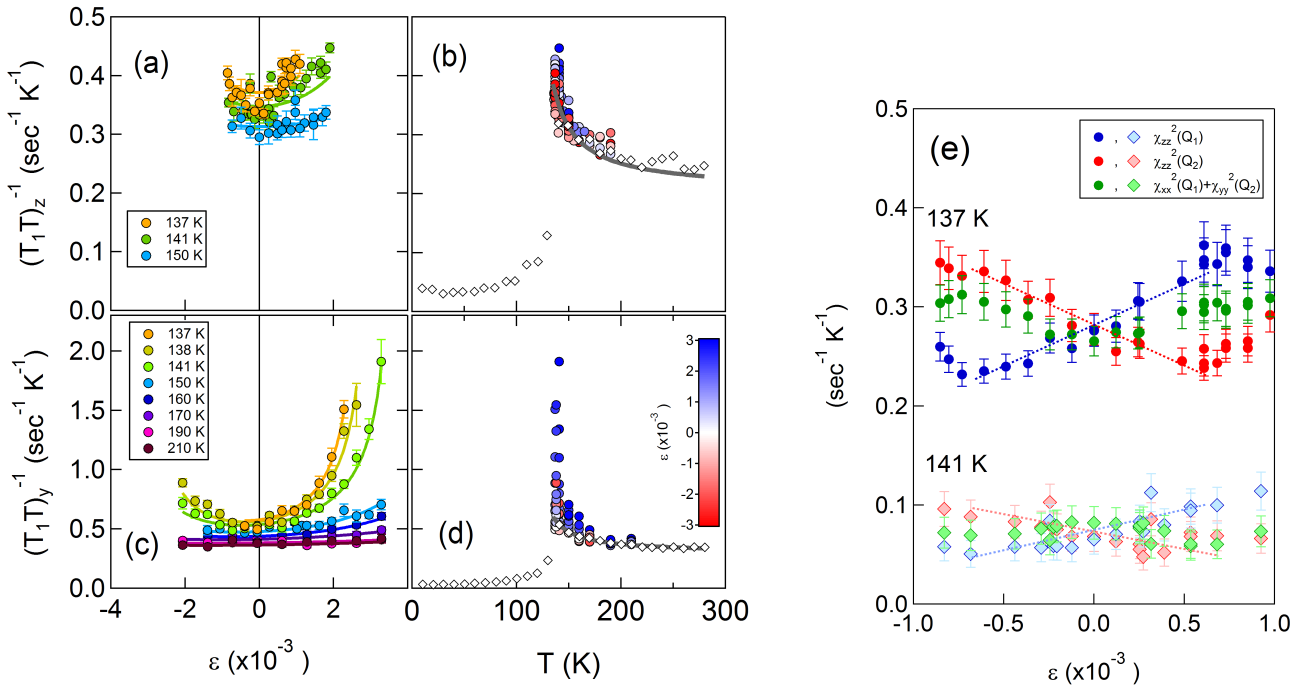

FIG. 3. $(T_1T)^{-1}_{y,z}$ versus strain (a,c) and versus temperature (b,d) The solid lines are fits as described in the text. The open diamonds in (b,d) are reproduced from Ref. 20. (e) $\chi_{zz}(\mathbf{Q}_1)$, $\chi_{zz}(\mathbf{Q}_2)$, and $\chi_{xx}(\mathbf{Q}_1)+\chi_{yy}(\mathbf{Q}_2)$ as a function of strain at 137K and 141K. The data have been displaced vertically for clarity. The dashed lines are guides to the eye.

$\mathbf{H}_0$. In our device, strain is always applied along the x axis defined in Fig. 2; since the b axis is defined as the shorter axis, positive (i.e. tensile) strain corresponds to $x \parallel a$ and $y \parallel b$, whereas negative (i.e. compressive) strain gives $y \parallel a$ and $x \parallel b$. When the crystal is strained by applying voltage to the piezoelectric stacks, the displacement, x, is measured by a capacitive position sensor, and strain is calculated as $\epsilon = (x - x_0)/L_0$, where L_0 is the unstrained length of the crystal. To account for differential thermal contraction, the zero-strain displacement, x_0, was determined by the condition that the quadrupolar splitting $\nu_{\alpha\alpha}$ satisfies the tetragonal-symmetry relationship $|\nu_{xx}| = |\nu_{yy}| = |\nu_{zz}|/2$, as described in the supplemental material. The linear relationship between $\nu_{\alpha\alpha}$ and strain (Fig. S1) indicates that both positive and negative strains are achieved, without bowing of the crystal. The field $\mathbf{H}_0$ was oriented either along the z direction parallel to the crystalline c axis, or in the plane of the crystal along the y-direction, as shown in Fig. 2.

The spin lattice relaxation rate $(T_1T)^{-1}_\mu$ for different field orientations $\mu = z, y$ is shown in Fig. 3 both as a function of strain ε and temperature T. It is striking that while $(T_1T)^{-1}_z$ increases by approximately 30% at 137K for the largest applied strain (approximatelly 0.3%), $(T_1T)^{-1}_y$ increases by 500%. In both cases, both positive and negative strain increase $(T_1T)^{-1}$ in a nonlinear fashion. This behavior is a manifestation of the spin anisotropy induced by nematic order. More precisely, the spin lattice relaxation rate is primarily dominated by the fluctuations of the local hyperfine field at the As site, which in turn is determined by the neighboring iron spins according to:

$$\left(\frac{1}{T_1T}\right)_\mu = \frac{\gamma^2}{2}\lim_{\omega\to 0}\sum_{\mathbf{q},\alpha,\beta}\mathcal{F}^{(\mu)}_{\alpha\beta}(\mathbf{q})\frac{\mathrm{Im}\chi_{\alpha\beta}(\mathbf{q},\omega)}{\hbar\omega}, \quad (1)$$

where γ is the nuclear gyromagnetic factor, $\mathcal{F}^{(\mu)}_{\alpha\beta}$ are the hyperfine form factors, which depend on the field direction μ (see Supplemental Material), $\chi_{\alpha\beta}(\mathbf{q},\omega)$ is the dynamical magnetic susceptibility, and $\alpha, \beta = \{x, y, z\}$ [17]. Because the system is metallic, spin fluctuations experience Landau damping, resulting in the low-energy dynamics $\chi^{-1}_{\alpha\beta}(\mathbf{q},\omega) = \chi^{-1}_{\alpha\beta}(\mathbf{q}) - i\hbar\omega/\Gamma$, where Γ is the Landau damping, as seen by neutron scattering experiments. Consequently, $\lim_{\omega\to 0}\frac{\mathrm{Im}\chi_{\alpha\beta}(\mathbf{q},\omega)}{\hbar\omega} = \frac{1}{\Gamma}\chi^2_{\alpha\beta}(\mathbf{q})$, i.e. the spin-lattice relaxation rate is proportional to the squared susceptibility integrated over the entire Brillouin zone. Since the magnetically ordered state has wavevectors $\mathbf{Q}_1 = (\pi, 0)$ and $\mathbf{Q}_2 = (0, \pi)$, one expects that the susceptibility is peaked at these two momenta. Indeed, neutron scattering experiments confirm that the magnetic spectral weight is strongly peaked at $\mathbf{Q}_1$ and $\mathbf{Q}_2$.

Therefore, as an initial step to elucidate the effect of strain on the spin fluctuations anisotropy, we consider that the susceptibility is sharply peaked at these two

magnetic ordering vectors. Evaluation of the hyperfine form factors yields:

$$\begin{aligned}(T_1T)_x^{-1} &\propto \chi_{xx}^2(\mathbf{Q}_1)+\chi_{yy}^2(\mathbf{Q}_2)+\chi_{zz}^2(\mathbf{Q}_2)\\ (T_1T)_y^{-1} &\propto \chi_{xx}^2(\mathbf{Q}_1)+\chi_{yy}^2(\mathbf{Q}_2)+\chi_{zz}^2(\mathbf{Q}_1)\\ (T_1T)_z^{-1} &\propto \chi_{zz}^2(\mathbf{Q}_1)+\chi_{zz}^2(\mathbf{Q}_2)\end{aligned} \quad (2)$$

where the prefactors are approximately the same in all equations (see SM), and proportional to the off-diagonal hyperfine matrix element $\mathcal{F}_{xz}$ coupling in-plane Fe spin fluctuations to out-of-plane As hyperfine fields (and vice-versa). The fact that $\chi_{zz}(\mathbf{Q}_i)$ contributes to T_1 for all directions of the applied magnetic field is thus consistent with the hyperfine field analysis depicted in Fig. 1, since out-of-plane spin fluctuations on the Fe sites produce hyperfine fluctuating fields in the As sites along both in-plane directions. Similarly, the fact that only $\chi_{xx}(\mathbf{Q}_1)$ and $\chi_{yy}(\mathbf{Q}_2)$ contribute to T_1 for external fields applied along the plane is a consequence of the fact that these spin fluctuations generate hyperfine fields in the As site oriented out of the plane.

Because by symmetry $(T_1T)_x^{-1}(\varepsilon) = (T_1T)_y^{-1}(-\varepsilon)$, the NMR data can be used to extract the strain and temperature dependence of the three polarized spin-susceptibility combinations $\chi_{zz}^2(\mathbf{Q}_1)$, $\chi_{zz}^2(\mathbf{Q}_2)$, and $\chi_{xx}^2(\mathbf{Q}_1)+\chi_{yy}^2(\mathbf{Q}_2)$, as shown in Fig. 3(e). This analysis provides several interesting insights. First, focusing on the out-of-plane fluctuations, in-plane strain enhances spin fluctuations around one of the two ordering vectors ($\chi_{zz}(\mathbf{Q}_1)$ for $\varepsilon>0$ and $\chi_{zz}(\mathbf{Q}_2)$ for $\varepsilon<0$) at the same time as it suppresses the fluctuations around the other ordering vector. Therefore, in-plane strain transfers magnetic spectral weight between the two dominant out-of-plane spin-fluctuation channels. This is consistent with neutron scattering experiments in detwinned pnictides [6], which however only probed the unpolarized susceptibility. More importantly, this behavior is a direct manifestation of the response of the nematic order parameter φ_{zz} to strain, since $\varphi_{zz}=\chi_{zz}^{-1}(\mathbf{Q}_2)-\chi_{zz}^{-1}(\mathbf{Q}_1)$.

Turning now to the average in-plane fluctuations $\chi_{xx}^2(\mathbf{Q}_1)+\chi_{yy}^2(\mathbf{Q}_2)$, we note that, in contrast to the quantity $\chi_{zz}(\mathbf{Q}_1)-\chi_{zz}(\mathbf{Q}_2)$, it is an even function of the applied strain. This behavior can be attributed to the response of the nematic order parameter $\varphi_{xy}=\chi_{xx}^{-1}(\mathbf{Q}_2)-\chi_{yy}^{-1}(\mathbf{Q}_1)$ to strain. Similarly to φ_{zz}, φ_{xy} promotes a transfer of magnetic spectral weight, but now between x-polarized spin fluctuations around $\mathbf{Q}_1$ and y-polarized spin fluctuations around $\mathbf{Q}_2$. Since only the combination $\chi_{xx}^2(\mathbf{Q}_1)+\chi_{yy}^2(\mathbf{Q}_2)$ contributes to the spin-lattice relation rate, the total magnetic spectral weight remains the same to linear order in φ_{xy}, since what is suppressed in, say, $\chi_{yy}(\mathbf{Q}_2)$ is tranferred to $\chi_{xx}(\mathbf{Q}_1)$. Of course, as strain is enhanced, non-linear effects quadratic in φ_{xy}^2 take place, in agreement with the behavior displayed by Fig. 3(e). Note that the third nematic order parameter, $\varphi_{yx}=\chi_{yy}^{-1}(\mathbf{Q}_2)-\chi_{xx}^{-1}(\mathbf{Q}_1)$, does not affect the in-plane fluctuations that contribute the most to the spin-lattice relaxation rate. This is not unexpected, since the spin fluctuations associated with $\chi_{yy}(\mathbf{Q}_1)$ and $\chi_{xx}(\mathbf{Q}_2)$ do not generate hyperfine fields in the As sites, as shown in Fig. 1.

The most striking feature of Fig. 3(e) is that the out-of-plane spin fluctuations seem to have a larger response to in-plane strain than the in-plane spin fluctuations. This observation suggests that the nematic susceptibility associated with φ_{zz}, $\chi_{\rm nem}^{(zz)}\equiv\partial\varphi_{zz}/\partial\varepsilon$, is larger than the nematic susceptibility associated with φ_{xy}, $\chi_{\rm nem}^{(xy)}\equiv\partial\varphi_{xy}/\partial\varepsilon$, and is manifestation of the fact that nematic order induces not only real-space anisotropy, but also spin-space anisotropy. To make this analysis more quantitative, we fit the full temperature, strain, and field orientation dependence of T_1 to a model that incorporates the fact that the magnetic fluctuations are not infinitely peaked at the ordering vectors $\mathbf{Q}_{1,2}$, since the magnetic correlation length is finite above the magnetic transition. In the tetragonal phase, there are three different magnetic correlation lengths, ξ_x, ξ_y, and ξ_z, associated respectively with the pairs of peaks $(\chi_{xx}(\mathbf{Q}_1),\chi_{yy}(\mathbf{Q}_2))$; $(\chi_{yy}(\mathbf{Q}_1),\chi_{xx}(\mathbf{Q}_2))$, and $(\chi_{zz}(\mathbf{Q}_1),\chi_{zz}(\mathbf{Q}_2))$. This spin anisotropy is intrinsic to the tetragonal crystalline symmetry and is enforced by the spin-orbit coupling even in the absence of nematic order. Nematic order induced by strain breaks the equivalence between these pairs of peaks, splitting the correlation lengths into $\tilde{\xi}_x^{-2}=\xi_x^{-2}\mp\varphi_{xy}$, $\tilde{\xi}_y^{-2}=\xi_y^{-2}\mp\varphi_{yx}$, and $\tilde{\xi}_z^{-2}=\xi_z^{-2}\mp\varphi_{zz}$. This model is similar to the one used previously in [15] and is described in the supplemental material.

The fits for $(T_1T)_z^{-1}$ and $(T_1T)_y^{-1}$ in the absence of strain are shown as solid gray lines in Figs. 3(b) and (d) for $\xi_x=\xi_y$. We find $\xi_z/\xi_x=0.88$, in agreement with the fact that in the absence of strain the spins point along the plane. Moreover, the temperature dependence of $\xi_x(T)$, shown in Fig. 4(a), gives values consistent with those measured by inelastic neutron scattering. Having fixed the unstrained parameters, we perform fits in the presence of strain, shown by the solid lines in Fig. 3(a) and (c). The only parameters introduced in this case are the nematic order parameters $\varphi_{xy}=\varphi_{yx}$ and φ_{zz}. The good agreement between the fitted and the experimental curves of both $(T_1T)_z^{-1}$ and $(T_1T)_y^{-1}$ over a wide temperature-strain regime demonstrates the suitability of the phenomenological model employed in our analysis.

The temperature and strain behaviors of the nematic order parameters $\varphi_{\alpha\beta}$ allows us to extract the temperature dependence of the nematic susceptibilities $\chi_{\rm nem}^{(xy)}$ and $\chi_{\rm nem}^{(zz)}$, as shown in Fig. 4(b). It is clear that generally $\chi_{\rm nem}^{(zz)}>\chi_{\rm nem}^{(xy)}$, particularly close to the magnetic transition. This quantitative analysis corroborates the qualitative conclusion above, namely that nematic order induces anisotropies in spin-space, and that the out-of-

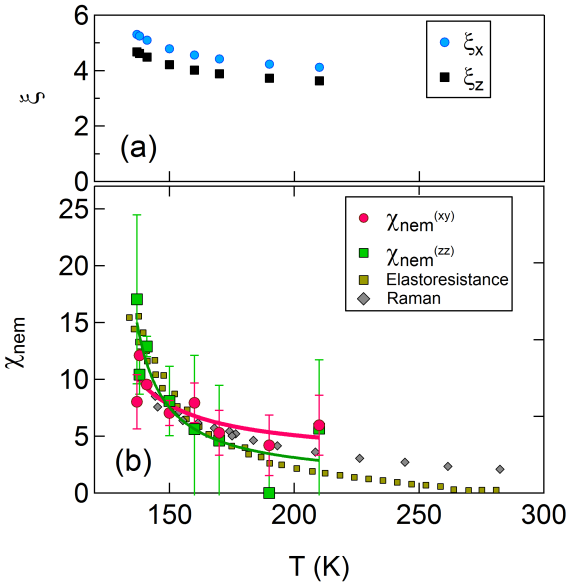

FIG. 4. Fit parameters (a) $\kappa_{zz,yx}/\kappa_{xy}$, and (b) ξ and κ_{xy} versus temperature, based on the fits (solid lines) shown in Fig. 3. Also shown are the nematic susceptibilities measured by Raman and elastoresistance measurements, reproduced from Refs. 21 and 22 and 23, respectively. The solid lines are fits as described in the text.

plane spin fluctuations are more strongly enhanced by in-plane strain than the in-plane spin fluctuations. It is interesting to compare $\chi^{(xy)}_{\rm nem}$ and $\chi^{(zz)}_{\rm nem}$ with the nematic susceptibility extracted from elastoresistance [23] and from electronic Raman spectroscopy experiments [21]. As shown in Fig. 4(b), the values are consistent, and the NMR-extracted nematic susceptibilities also follow a Curie-Weiss type of behavior [22], with a Curie temperature $T_0 = 116$ K comparable to that extracted from the elastoresistance [23]. Note however that, in contrast to our NMR analysis, the other probes for the nematic susceptibility are not sensitive to the "polarization" of the nematic susceptibility.

To the best of our knowledge, our results are the first to reveal the internal spin structure of the nematic order parameter in iron-based superconductors. This behavior is a clear manifestation of the entanglement between spin, orbital, and lattice degrees of freedom in the normal state of these compounds. Since superconductivity emerges from this unique state, the rich interplay between these different degrees of freedom revealed by our NMR analysis will certainly affect the properties of the superconducting state.

The surprising anisotropic response of different nematic components to in-plane strain reveals that the spin polarization can be controlled by lattice distortions, similar to a piezomagnetic effect. In particular, the result $\chi^{(zz)}_{\rm nem} > \chi^{(xy)}_{\rm nem}$ implies that for sufficiently large strain ε^*, the dominant spin polarization will shift from in-plane to out-of-plane. The value of ε^* can be estimated from the condition that the out-of-plane magnetic correlation length $\tilde{\xi}_z = \xi_z - \varepsilon\chi^{(zz)}_{\rm nem}$ becomes larger than the in-plane magnetic correlation length $\tilde{\xi}_x = \xi_x - \varepsilon\chi^{(xy)}_{\rm nem}$, yielding $\varepsilon^* \approx 0.4\%$ close to the magnetic transition temperature. Such a strain value, which is just beyond the capability of our specific piezo device, can reasonably be achieved by similar types of devices, however. More importantly, this analysis opens a new avenue to control spin polarization in nematic materials without using magnetic fields, but instead by using mechanical strain. Since nematic order has been observed in other correlated materials such as cuprates and ruthenates, it will be interesting to investigate whether similar sizable effects are present in these systems as well.

More broadly, our work demonstrates that precision tunable strain in combination with NMR provides a novel and important method to probe spin and charge degrees of freedom. It provides an intriguing possibility to tune the NMR spin relaxation rate by changing a voltage bias on the piezoelectric stacks. The subtle coupling between the lattice and spin polarizations exhibited by $BaFe_2As_2$ offers the potential for controlling magnetic properties through lattice deformations in next generation materials. Another potential application of our technique is the use of nuclear quadrupolar resonance to image local strains. The large response of the EFG to strain observed in this study would translate into high spatial resolution in a linear strain gradient, so that As NMR may be able to resolve microscopic features such as grain boundaries or defects.

ACKNOWLEDGEMENTS

We thank A. Dioguardi, S. Kivelson, and I. Fisher for enlightening discussions, and P. Klavins, for assistance in the laboratory. Work at UC Davis was supported by the NSF under Grant No. DMR-1506961. RMF is supported by the U. S. Department of Energy, Office of Science, Basic Energy Sciences, under award number DE-SC0012336. R. Sarkar was partially supported by the DFG through SFB 1143 for the project C02. Work done at Ames Lab (SLB, PCC, MT, RP, EIT) was supported by the U.S. Department of Energy, Office of Basic Energy Science, Division of Materials Sciences and Engineering. Ames Laboratory is operated for the U.S. Department of Energy by Iowa State University under Contract No. DE-AC02-07CH11358.

METHODS

Crystals were grown in self-flux as described in [24] and cut along the $(110)_{\rm T}$ direction. Sample A had a

mass of 2.52 mg and was mounted with the field parallel to the **c** axis, and Sample B had a mass 0.91 mg and was mounted with the field perpendicular to the **c** axis (see Fig. 2). The crystals were secured with heat-cured epoxy (UHU Plus 300 epoxy resin). Strain was applied along the $(110)_{\mathrm{T}}$ direction using the CS100 cryogenic uniaxial strain cell developed by Razorbill Instruments based on a design by Hicks et. al. [18], mounted in a modified probe operating in a Quantum Design PPMS cryostat. The displacement, x was measured by monitoring the capacitance of using a precision capacitance bridge with a resolution of 0.1nm. The strain was computed as $\epsilon = (x - x_0)/L_0$, where $L_0 = 2.052$ mm and $x_0 = 49.5$ μm for sample A and $L_0 = 1.494$ mm and $x_0 = 51.58$ μm for sample B. For sample B, positive (tensile) strain corresponds to $\mathbf{H}_0 \,||\, \hat{b}$ and negative (compressive) strain corresponds to $\mathbf{H}_0 \,||\, \hat{a}$. Because the sample was mounted at room temperature, thermal contraction creates positive strain even at zero piezo bias at low temperatures, making a precise determination of x_0 difficult. For sample A x_0 was determined by the minimum in $(T_1T)^{-1}$ versus x, and for sample B x_0 was determined by the value $\nu_{bb}(x_0) = |\nu_{cc}|/2 = 1.23$ MHz, where $\nu_{\alpha\alpha}$ is the quadrupolar splitting for field along the α direction (see supplemental materials). The maximum/minimum possible applied voltages to the piezoelectric stacks limited the range of strains that could be applied to between approximately -0.002 to $+0.003$ in the perpendicular case, and -0.0015 to $+0.002$ for the parallel case. The spin-lattice relaxation rate was measured using inversion recovery at the central transition in fixed field, and the data were fit to the expression $M(t) = M_0\left[1 - 2f\left(\frac{9}{10}e^{-6t/T_1} + \frac{1}{10}e^{-t/T_1}\right)\right]$. The data were well-fit to a single T_1 value.

[1] Paul C. Canfield and Sergey L. Bud'ko, "FeAs-based superconductivity: A case study of the effects of transition metal doping on $BaFe_2As_2$," Annu. Rev. Condens. Matter Phys. **1**, 27–50 (2010).

[2] R. M. Fernandes, A. V. Chubukov, J. Knolle, I. Eremin, and J. Schmalian, "Preemptive nematic order, pseudogap, and orbital order in the iron pnictides," Phys. Rev. B **85**, 024534 (2012).

[3] Rafael M Fernandes and Jrg Schmalian, "Manifestations of nematic degrees of freedom in the magnetic, elastic, and superconducting properties of the iron pnictides," Supercond. Sci. Technol. **25**, 084005 (2012).

[4] Rafael M. Fernandes, Anna E. Böhmer, Christoph Meingast, and Jörg Schmalian, "Scaling between magnetic and lattice fluctuations in iron pnictide superconductors," Phys. Rev. Lett. **111**, 137001 (2013).

[5] E. C. Blomberg, A. Kreyssig, M. A. Tanatar, R. M. Fernandes, M. G. Kim, A. Thaler, J. Schmalian, S. L. Bud'ko, P. C. Canfield, A. I. Goldman, and R. Prozorov, "Effect of tensile stress on the in-plane resistivity anisotropy in $BaFe_2As_2$," Phys. Rev. B **85**, 144509 (2012).

[6] Xingye Lu, J. T. Park, Rui Zhang, Huiqian Luo, Andriy H. Nevidomskyy, Qimiao Si, and Pengcheng Dai, "Nematic spin correlations in the tetragonal state of uniaxial-strained $BaFe_{2-x}Ni_xAs_2$," Science **345**, 657 – 660 (2014).

[7] Haoran Man, Xingye Lu, Justin S. Chen, Rui Zhang, Wenliang Zhang, Huiqian Luo, J. Kulda, A. Ivanov, T. Keller, Emilia Morosan, Qimiao Si, and Pengcheng Dai, "Electronic nematic correlations in the stress-free tetragonal state of $BaFe_{2-x}Ni_xAs_2$," Phys. Rev. B **92**, 134521 (2015).

[8] Eduardo Fradkin, Steven A. Kivelson, Michael J. Lawler, James P. Eisenstein, and Andrew P. Mackenzie, "Nematic fermi fluids in condensed matter physics," Annu. Rev. Condens. Matter Phys. **1**, 153–178 (2010).

[9] M. A. Tanatar, E. C. Blomberg, A. Kreyssig, M. G. Kim, N. Ni, A. Thaler, S. L. Bud'ko, P. C. Canfield, A. I. Goldman, I. I. Mazin, and R. Prozorov, "Uniaxial-strain mechanical detwinning of $CaFe_2As_2$ and $BaFe_2As_2$ crystals: Optical and transport study," Phys. Rev. B **81**, 184508 (2010).

[10] Jiun-Haw Chu, James G. Analytis, Kristiaan De Greve, Peter L. McMahon, Zahirul Islam, Yoshihisa Yamamoto, and Ian R. Fisher, "In-plane resistivity anisotropy in an underdoped iron arsenide superconductor," Science **329**, 824–826 (2010).

[11] R. M. Fernandes, A. V. Chubukov, and J. Schmalian, "What drives nematic order in iron-based superconductors?" Nat. Phys. **10**, 97–104 (2014).

[12] Pengcheng Dai, "Antiferromagnetic order and spin dynamics in iron-based superconductors," Rev. Mod. Phys. **87**, 855–896 (2015).

[13] Yu Song, Xingye Lu, D. L. Abernathy, David W. Tam, J. L. Niedziela, Wei Tian, Huiqian Luo, Qimiao Si, and Pengcheng Dai, "Energy dependence of the spin excitation anisotropy in uniaxial-strained $BaFe_{1.9}Ni_{0.1}As_2$," Phys. Rev. B **92**, 180504 (2015).

[14] A. P. Dioguardi, M. M. Lawson, B. T. Bush, J. Crocker, K. R. Shirer, D. M. Nisson, T. Kissikov, S. Ran, S. L. Bud'ko, P. C. Canfield, S. Yuan, P. L. Kuhns, A. P. Reyes, H.-J. Grafe, and N. J. Curro, "NMR evidence for inhomogeneous glassy behavior driven by nematic fluctuations in iron arsenide superconductors," Phys. Rev. B **92**, 165116 (2015).

[15] T. Kissikov, A. P. Dioguardi, E. I. Timmons, M. A. Tanatar, R. Prozorov, S. L. Bud'ko, P. C. Canfield, R. M. Fernandes, and N. J. Curro, "NMR study of nematic spin fluctuations in a detwinned single crystal of underdoped $Ba(Fe_{1-x}Co_x)_2As_2$," Phys. Rev. B **94**, 165123 (2016).

[16] F. L. Ning, M. Fu, D. A. Torchetti, T. Imai, A. S. Sefat, P. Cheng, B. Shen, and H.-H. Wen, "Critical behavior of the spin density wave transition in underdoped $Ba(Fe_{1-x}Co_x)_2As_2$ ($x \leq 0.05$): ^{75}As NMR investigation," Phys. Rev. B **89**, 214511 (2014).

[17] Andrew Smerald and Nic Shannon, "Angle-resolved NMR: Quantitative theory of ^{75}As T_1 relaxation rate in $BaFe_2As_2$," Phys. Rev. B **84**, 184437 (2011).

[18] Clifford W. Hicks, Mark E. Barber, Stephen D. Edkins, Daniel O. Brodsky, and Andrew P. Mackenzie, "Piezoelectric-based apparatus for strain tuning," Rev. Sci. Instrum. **85**, 065003 (2014).

[19] C. W. Hicks, D. O. Brodsky, E. A. Yelland, A. S. Gibbs, J. A. N. Bruin, M. E. Barber, S. D. Edkins, K. Nishimura,

S. Yonezawa, Y. Maeno, and A. P. Mackenzie, "Strong increase of T_c of Sr_2RuO_4 under both tensile and compressive strain," Science **344**, 283–285 (2014).
[20] Kentaro Kitagawa, Naoyuki Katayama, Kenya Ohgushi, Makoto Yoshida, and Masashi Takigawa, "Commensurate itinerant antiferromagnetism in $BaFe_2As_2$: ^{75}As-NMR studies on a self-flux grown single crystal," J. Phys. Soc. Jpn. **77**, 114709 (2008).
[21] Y. Gallais, R. M. Fernandes, I. Paul, L. Chauvière, Y.-X. Yang, M.-A. Méasson, M. Cazayous, A. Sacuto, D. Colson, and A. Forget, "Observation of incipient charge nematicity in $Ba(Fe_{1-x}Co_x)_2As_2$," Phys. Rev. Lett. **111**, 267001 (2013).
[22] Yann Gallais and Indranil Paul, "Charge nematicity and electronic raman scattering in iron-based superconductors," C. R. Phys. **17**, 113–139 (2016).
[23] Jiun-Haw Chu, Hsueh-Hui Kuo, James G. Analytis, and Ian R. Fisher, "Divergent nematic susceptibility in an iron arsenide superconductor," Science **337**, 710–712 (2012).
[24] N. Ni, M. E. Tillman, J.-Q. Yan, A. Kracher, S. T. Hannahs, S. L. Bud'ko, and P. C. Canfield, "Effects of Co substitution on thermodynamic and transport properties and anisotropic H_{c2} in $Ba(Fe_{1-x}Co_x)_2As_2$ single crystals," Phys. Rev. B **78**, 214515 (2008).
[25] A. P. Dioguardi, T. Kissikov, C. H. Lin, K. R. Shirer, M. M. Lawson, H.-J. Grafe, J.-H. Chu, I. R. Fisher, R. M. Fernandes, and N. J. Curro, "NMR evidence for inhomogeneous nematic fluctuations in $BaFe_2(As_{1-x}P_x)_2$," Phys. Rev. Lett. **116**, 107202 (2016).
[26] Tetsuya Iye, Marc-Henri Julien, Hadrien Mayaffre, Mladen Horvatič, Claude Berthier, Kenji Ishida, Hiroaki Ikeda, Shigeru Kasahara, Takasada Shibauchi, and Yuji Matsuda, "Emergence of orbital nematicity in the tetragonal phase of $BaFe_2(As_{1-x}P_x)_2$," J. Phys. Soc. Jpn. **84**, 043705 (2015).
[27] F. L. Ning, K. Ahilan, T. Imai, A. S. Sefat, R. Jin, M. A. McGuire, B. C. Sales, and D. Mandrus, "^{59}Co and ^{75}As NMR investigation of lightly doped $Ba(Fe_{1-x}Co_x)_2As_2$ ($x = 0.02, 0.04$)," Phys. Rev. B **79**, 140506 (2009).
[28] A. P. Dioguardi, N. apRoberts Warren, A. C. Shockley, S. L. Bud'ko, N. Ni, P. C. Canfield, and N. J. Curro, "Local magnetic inhomogeneities in $Ba(Fe_{1-x}Ni_x)_2As_2$ as seen via As-75 NMR," Phys. Rev. B **82**, 140411(R) (2010).
[29] Hikaru Takeda, Takashi Imai, Makoto Tachibana, Jonathan Gaudet, Bruce D. Gaulin, Bayrammurad I. Saparov, and Athena S. Sefat, "Cu substitution effects on the local magnetic properties of $Ba(Fe_{1-x}Cu_x)_2As_2$: A site-selective ^{75}As and ^{63}Cu NMR study," Phys. Rev. Lett. **113**, 117001 (2014).
[30] S-H. Baek, D. V. Efremov, J. M. Ok, J. S. Kim, Jeroen van den Brink, and B. Büchner, "Orbital-driven nematicity in FeSe," Nat. Mater. **14**, 210–214 (2015).
[31] Mingquan He, Liran Wang, Felix Ahn, Frdric Hardy, Thomas Wolf, Peter Adelmann, Jrg Schmalian, Ilya Eremin, and Christoph Meingast, "Dichotomy between in-plane magnetic susceptibility and resistivity anisotropies in extremely strained $BaFe_2As_2$," 1610.05575v2.
[32] Morten H. Christensen, Jian Kang, Brian M. Andersen, Ilya Eremin, and Rafael M. Fernandes, "Spin reorientation driven by the interplay between spin-orbit coupling and hund's rule coupling in iron pnictides," Phys. Rev. B **92**, 214509 (2015).

SPECTRAL MEASUREMENTS

When the crystal is strained by applying voltage to the piezoelectric stacks, the displacement, x, is measured by a capacitive position sensor, and strain is calculated as $\epsilon = (x - x_0)/L_0$, where L_0 is the unstrained length of the crystal. It is crucial to determine the unstrained displacement, x_0, at cryogenic temperatures due to differential thermal contraction between the strain device and the sample. This value can be obtained by observing the asymmetry of the electric field gradient (EFG) tensor. The spectra were measured by acquiring echoes while sweeping the magnetic field H_0 at fixed frequency. The quadrupolar satellite resonances occur at fields $H_{sat} = (f_0 \pm \nu_{\alpha\alpha})/\gamma(1 + K_{\alpha\alpha})$, where f_0 is the radiofrequency, $\gamma = 7.29019$ MHz/T is the gyromagnetic ratio, $K_{\alpha\alpha}$ and $\nu_{\alpha\alpha}$ are the Knight shift and EFG tensor components in the $\alpha = (x, y, z)$ direction. The central transition field is given by: $H_{cen} = \frac{f_0}{\gamma(1+K_{\alpha\alpha})}\left(\frac{1}{2} + \sqrt{\frac{3f_0^2 - 2(\nu_{\beta\beta}+\nu_{\alpha\alpha})^2}{12}}\right)$, where $\beta = (y, x, z)$ for $\alpha = x, y, z$. The center of gravity of each peak was used to determine the resonance field, and hence $K_{\alpha\alpha}$ and $\nu_{\alpha\alpha}$ as a function of strain.

Fig. 5(b) shows a typical field-swept NMR spectrum of the ^{75}As, revealing a narrow central transition ($I_z = 1/2 \leftrightarrow -1/2$) and two quadrupolar satellite peaks ($\pm 3/2 \leftrightarrow \pm 1/2$). The spectrum was fit to the sum of three Gaussians to extract both the Knight shift, $K_{\alpha\alpha}$, and the EFG, $\nu_{\alpha\alpha}$. The EFG tensor is given by $\nu_{\alpha\beta} = (eQ/12h)\partial^2 V/\partial x_\alpha \partial x_\beta$, where Q is the quadrupolar moment of the ^{75}As and V is the electrostatic potential at the As site. This quantity is dominated by the occupation of the $d_{xz,yz}$-orbitals of the neighboring Fe atoms, and the EFG asymmetry $\eta = (\nu_{yy} - \nu_{xx})/(\nu_{xx} + \nu_{yy})$ is a measure of the nematic order parameter [25, 26]. Note that the magnetic field lies along the shorter b-axis under tensile strain ($\epsilon > 0$), and along the longer a-axis under compressive strain ($\epsilon < 0$), as shown in Fig. 2 of the main text. The EFG enables us to identify the zero-strain displacement, x_0, by the condition $|\nu_{xx}| = |\nu_{yy}| = |\nu_{zz}|/2$. As shown in Fig. 5(c), ν_{yy}, and hence $\eta(\epsilon) = (\nu_{yy}(\epsilon) - \nu_{yy}(-\epsilon))/(\nu_{yy}(\epsilon) + \nu_{yy}(-\epsilon))$, varies linearly with strain.

Despite the fact that the EFG varies with strain, we find no significant variation of the satellite linewidth with strain. The strong variation of the EFG with strain explains the quadrupolar broadening observed in Co, Ni or Cu-doped $Ba(Fe,M)_2As_2$ [27–29]. The dopant atoms create an inhomogeneous strain field that gives rise to a distribution of local EFGs. Recently a finite value of $\eta \sim 0.1$ was reported in the tetragonal phase of unstrained $BaFe_2(As_{1-x}P_x)_2$ above T_s [26]. The origin of this finite nematicity is likely due to local defects, and

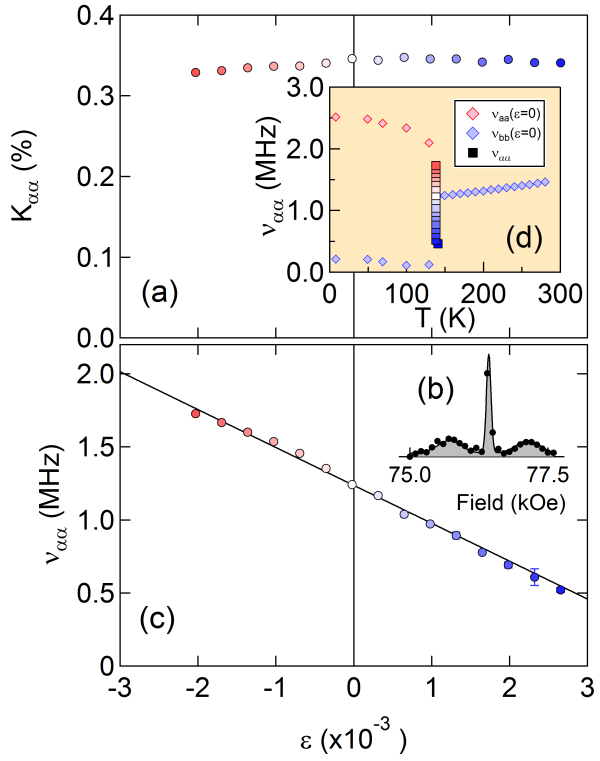

FIG. 5. (a) Knight shift versus strain at 138K. (b) The ^{75}As spectrum at 138K for a strain level of 0.0265% at frequency 55.924 MHz. The solid line is a fit to the spectrum as described in the text. (c) The quadrupolar splitting versus strain, and (d) versus temperature. The zero-strain points (diamonds) are reproduced from Ref. 20.

based on our results the strain fields are on the order of 0.05%.

The Knight shift is shown versus strain in Fig. 5(a) for $\mathbf{H}_0 \perp c$. The in-plane Knight shift shows little or no variation with ϵ, such that $(K_{xx} - K_{yy})/K_{yy} \leq 3\%$ at the highest strain levels in this material. This result is surprising because the same quantity is approximately 6% in the nematic phase of FeSe [30]. Recent static susceptibility measurements in $BaFe_2As_2$ under strain indicate that χ_{xx} and χ_{yy} in the paramagnetic phase differ by only 5% [31]. This result suggests that $\chi_{\alpha\alpha}(\mathbf{q}=0)$ couples only weakly to the strain.

SPIN-LATTICE RELAXATION RATE: MODEL

As stated in the main text, the spin-lattice relaxation rate is given by:

$$\left(\frac{1}{T_1T}\right)_\mu = \frac{\gamma^2}{2}\sum_{\mathbf{q},\alpha,\beta}\mathcal{F}^{(\mu)}_{\alpha\beta}(\mathbf{q})\frac{\mathrm{Im}\chi_{\alpha\beta}(\mathbf{q},\omega)}{\hbar\omega} \tag{3}$$

where γ is the gyromagnetic ratio of the nuclear spin, and $\mathcal{F}^{(\mu)}_{\alpha\beta}$ is a form factor that depends on the direction of the applied field (indicated by μ), and $\alpha,\beta = \{x,y,z\}$. The coordinate system is defined such that x and y connect nearest neighbor Fe atoms. Ref. [17] derived the form factor for an As nucleus subject to an arbitrary field direction. In the paramagnetic state, one obtains (see also Ref. [15]):

$$\left(\frac{1}{T_1T}\right)_\mu = \frac{\gamma^2}{2}\sum_{\mathbf{q}}\sum_{\alpha=1,2}\left[\bar{R}^{(\mu)}\cdot\bar{A}_{\mathbf{q}}\cdot\bar{\bar{\chi}}(\mathbf{q})\cdot\bar{A}^\dagger_{\mathbf{q}}\cdot\left(\bar{R}^{(\mu)}\right)^\dagger\right]_{\alpha\alpha} \tag{4}$$

All quantities with an overbar are 3×3 matrices. The matrix $\bar{\bar{\chi}}(\mathbf{q})$ is diagonal; its matrix elements are related to the magnetic susceptibility elements according to:

$$\tilde{\chi}_{\alpha\alpha}(\mathbf{q}) \equiv \lim_{\omega\to 0}\frac{\mathrm{Im}\chi_{\alpha\alpha}(\mathbf{q},\omega)}{\hbar\omega} = \frac{1}{\Gamma}\chi^2_{\alpha\alpha}(\mathbf{q}) \tag{5}$$

where Γ is the Landau damping term. Furthermore, we have the hyperfine tensor:

$$\bar{A}_{\mathbf{q}} = 4 \begin{pmatrix} A_{xx}\cos\left(\frac{q_x}{2}\right)\cos\left(\frac{q_y}{2}\right) & -A_{xy}\sin\left(\frac{q_x}{2}\right)\sin\left(\frac{q_y}{2}\right) & iA_{xz}\sin\left(\frac{q_x}{2}\right)\cos\left(\frac{q_y}{2}\right) \\ -A_{yx}\sin\left(\frac{q_x}{2}\right)\sin\left(\frac{q_y}{2}\right) & A_{yy}\cos\left(\frac{q_x}{2}\right)\cos\left(\frac{q_y}{2}\right) & iA_{yz}\cos\left(\frac{q_x}{2}\right)\sin\left(\frac{q_y}{2}\right) \\ iA_{zx}\sin\left(\frac{q_x}{2}\right)\cos\left(\frac{q_y}{2}\right) & iA_{zy}\cos\left(\frac{q_x}{2}\right)\sin\left(\frac{q_y}{2}\right) & A_{zz}\cos\left(\frac{q_x}{2}\right)\cos\left(\frac{q_y}{2}\right) \end{pmatrix} \tag{6}$$

and the rotation matrix:

$$\bar{R}^{(\mu)} = \begin{pmatrix} \sin^2\phi + \cos\theta\,\cos^2\phi & -\sin 2\phi\,\sin^2\frac{\theta}{2} & \cos\phi\,\sin\theta \\ -\sin 2\phi\,\sin^2\frac{\theta}{2} & \cos^2\phi + \cos\theta\,\sin^2\phi & \sin\phi\,\sin\theta \\ -\cos\phi\,\sin\theta & -\sin\phi\,\sin\theta & \cos\theta \end{pmatrix} \tag{7}$$

Here, the field direction μ is described by the angles θ, φ according to $\hat{\mathbf{h}} = \cos\varphi\sin\theta\,\hat{\mathbf{x}} + \sin\varphi\sin\theta\,\hat{\mathbf{y}} + \cos\theta\,\hat{\mathbf{z}}$. Because the lattice distortion is very small, we consider hereafter that the hyperfine tensor remains essentially tetragonal, i.e. $A_{xx} = A_{yy}$, $A_{yz} = A_{xz}$, and $A_{xy} = A_{yx}$.

It is now straightforward to obtain the expressions for $1/\left(T_1T\right)_\mu$ for different field directions μ. We find:

$$\begin{aligned} \left(\frac{1}{T_1T}\right)_x = {} & 8\gamma^2 \sum_{\mathbf{q}} \left[\sin^2\left(\frac{q_x}{2}\right)\sin^2\left(\frac{q_y}{2}\right)A_{xy}^2 + \sin^2\left(\frac{q_x}{2}\right)\cos^2\left(\frac{q_y}{2}\right)A_{xz}^2\right]\tilde{\chi}_{xx}\left(\mathbf{q}\right) \\ & 8\gamma^2 \sum_{\mathbf{q}} \left[\cos^2\left(\frac{q_x}{2}\right)\cos^2\left(\frac{q_y}{2}\right)A_{yy}^2 + \cos^2\left(\frac{q_x}{2}\right)\sin^2\left(\frac{q_y}{2}\right)A_{yz}^2\right]\tilde{\chi}_{yy}\left(\mathbf{q}\right) \\ & 8\gamma^2 \sum_{\mathbf{q}} \left[\cos^2\left(\frac{q_x}{2}\right)\sin^2\left(\frac{q_y}{2}\right)A_{yz}^2 + \cos^2\left(\frac{q_x}{2}\right)\cos^2\left(\frac{q_y}{2}\right)A_{zz}^2\right]\tilde{\chi}_{zz}\left(\mathbf{q}\right) \end{aligned} \tag{8}$$

$$\begin{aligned} \left(\frac{1}{T_1T}\right)_y = {} & 8\gamma^2 \sum_{\mathbf{q}} \left[\cos^2\left(\frac{q_x}{2}\right)\cos^2\left(\frac{q_y}{2}\right)A_{xx}^2 + \sin^2\left(\frac{q_x}{2}\right)\cos^2\left(\frac{q_y}{2}\right)A_{xz}^2\right]\tilde{\chi}_{xx}\left(\mathbf{q}\right) \\ & 8\gamma^2 \sum_{\mathbf{q}} \left[\sin^2\left(\frac{q_x}{2}\right)\sin^2\left(\frac{q_y}{2}\right)A_{xy}^2 + \cos^2\left(\frac{q_x}{2}\right)\sin^2\left(\frac{q_y}{2}\right)A_{yz}^2\right]\tilde{\chi}_{yy}\left(\mathbf{q}\right) \\ & 8\gamma^2 \sum_{\mathbf{q}} \left[\sin^2\left(\frac{q_x}{2}\right)\cos^2\left(\frac{q_y}{2}\right)A_{xz}^2 + \cos^2\left(\frac{q_x}{2}\right)\cos^2\left(\frac{q_y}{2}\right)A_{zz}^2\right]\tilde{\chi}_{zz}\left(\mathbf{q}\right) \end{aligned} \tag{9}$$

and:

$$\begin{aligned} \left(\frac{1}{T_1T}\right)_z = {} & 8\gamma^2 \sum_{\mathbf{q}} \left[\cos^2\left(\frac{q_x}{2}\right)\cos^2\left(\frac{q_y}{2}\right)A_{xx}^2 + \sin^2\left(\frac{q_x}{2}\right)\sin^2\left(\frac{q_y}{2}\right)A_{xy}^2\right]\tilde{\chi}_{xx}\left(\mathbf{q}\right) \\ & 8\gamma^2 \sum_{\mathbf{q}} \left[\cos^2\left(\frac{q_x}{2}\right)\cos^2\left(\frac{q_y}{2}\right)A_{yy}^2 + \sin^2\left(\frac{q_x}{2}\right)\sin^2\left(\frac{q_y}{2}\right)A_{xy}^2\right]\tilde{\chi}_{yy}\left(\mathbf{q}\right) \\ & 8\gamma^2 \sum_{\mathbf{q}} \left[\sin^2\left(\frac{q_x}{2}\right)\cos^2\left(\frac{q_y}{2}\right)A_{xz}^2 + \cos^2\left(\frac{q_x}{2}\right)\sin^2\left(\frac{q_y}{2}\right)A_{yz}^2\right]\tilde{\chi}_{zz}\left(\mathbf{q}\right) \end{aligned} \tag{10}$$

If we approximate the magnetic susceptibility as delta-functions peaked at the magnetic ordering vectors $\mathbf{Q}_1 = (\pi, 0)$ and $\mathbf{Q}_2 = (0, \pi)$, we obtain:

$$(T_1T)_x^{-1} = \frac{8\gamma^2 A_{xz}^2}{\Gamma}\left[\chi_{xx}^2\left(\mathbf{Q}_1\right) + \chi_{yy}^2\left(\mathbf{Q}_2\right) + \chi_{zz}^2\left(\mathbf{Q}_2\right)\right] \tag{11}$$

$$(T_1T)_y^{-1} = \frac{8\gamma^2 A_{xz}^2}{\Gamma}\left[\chi_{xx}^2\left(\mathbf{Q}_1\right) + \chi_{yy}^2\left(\mathbf{Q}_2\right) + \chi_{zz}^2\left(\mathbf{Q}_1\right)\right] \tag{12}$$

$$(T_1T)_z^{-1} = \frac{8\gamma^2 A_{xz}^2}{\Gamma}\left[\chi_{zz}^2\left(\mathbf{Q}_1\right) + \chi_{zz}^2\left(\mathbf{Q}_2\right)\right] \tag{13}$$

These equations can be inverted to extract the quantities:

$$\chi_{zz}^2\left(\mathbf{Q}_1\right) = \frac{\Gamma}{16\gamma^2 A_{xz}^2}\left[-(T_1T)_y^{-1}(-\epsilon) + (T_1T)_y^{-1}(\epsilon) + (T_1T)_z^{-1}(\epsilon)\right] \tag{14}$$

$$\chi_{zz}^2\left(\mathbf{Q}_2\right) = \frac{\Gamma}{16\gamma^2 A_{xz}^2}\left[(T_1T)_y^{-1}(-\epsilon) - (T_1T)_y^{-1}(\epsilon) + (T_1T)_z^{-1}(\epsilon)\right] \tag{15}$$

$$\chi_{xx}^2\left(\mathbf{Q}_1\right) + \chi_{yy}^2\left(\mathbf{Q}_2\right) = \frac{\Gamma}{16\gamma^2 A_{xz}^2}\left[(T_1T)_y^{-1}(-\epsilon) + (T_1T)_y^{-1}(\epsilon) - (T_1T)_z^{-1}(\epsilon)\right], \tag{16}$$

using the fact that $(T_1T)_x^{-1}(\epsilon) = (T_1T)_y^{-1}(-\epsilon)$. These quantities are plotted in Fig. 3(e) of the main text.

Although useful for a qualitative analysis, this approximation neglects the important fact that the magnetic fluctuations have finite correlation lengths ξ. To model this effect, we consider susceptibilities peaked at $\mathbf{Q}_1$ and $\mathbf{Q}_2$, as seen by neutron scattering experiments (the amplitude χ_0 of the susceptibilities is absorbed in Γ, for convenience) [6]:

$$\begin{aligned}
\Gamma\tilde{\chi}_{xx}(\mathbf{q}) &= \frac{1}{\left[\left(\xi_x^{-2}-\varphi_{xy}\right)+\left(\cos q_x-\cos q_y+2\right)\right]^2}+\frac{1}{\left[\left(\xi_y^{-2}+\varphi_{yx}\right)+\left(-\cos q_x+\cos q_y+2\right)\right]^2}\\
\Gamma\tilde{\chi}_{yy}(\mathbf{q}) &= \frac{1}{\left[\left(\xi_y^{-2}-\varphi_{yx}\right)+\left(\cos q_x-\cos q_y+2\right)\right]^2}+\frac{1}{\left[\left(\xi_x^{-2}+\varphi_{xy}\right)+\left(-\cos q_x+\cos q_y+2\right)\right]^2}\\
\Gamma\tilde{\chi}_{zz}(\mathbf{q}) &= \frac{1}{\left[\left(\xi_y^{-2}-\varphi_{zz}\right)+\left(\cos q_x-\cos q_y+2\right)\right]^2}+\frac{1}{\left[\left(\xi_y^{-2}+\varphi_{zz}\right)+\left(-\cos q_x+\cos q_y+2\right)\right]^2},
\end{aligned} \tag{17}$$

Note that we have three different correlation lengths: ξ_x corresponds to in-plane spin fluctuations with spins parallel to the ordering vector direction; ξ_y corresponds to in-plane spin fluctuations with spins perpendicular to the ordering vector direction; and ξ_z corresponds to out-of-plane spin fluctuations. This spin anisotropy originates from the spin-orbit coupling, as shown in Ref. [32]. The nematic order parameters $\varphi_{\alpha\beta}$ split the tetragonal degeneracy between $\chi_{xx}(\mathbf{Q}_1)$ and $\chi_{yy}(\mathbf{Q}_2)$, between $\chi_{xx}(\mathbf{Q}_2)$ and $\chi_{yy}(\mathbf{Q}_1)$, and between $\chi_{zz}(\mathbf{Q}_1)$ and $\chi_{zz}(\mathbf{Q}_2)$. They are related to the external strain ϵ according to the nematic susceptibilities $\chi_{\text{nem}}^{(\alpha\beta)}$, i.e. $\varphi_{\alpha\beta} = \epsilon\chi_{\text{nem}}^{(\alpha\beta)}$.

Substituting these expressions in Eqs. (8), (9), and (10) give:

$$\begin{aligned}
\frac{\Gamma}{8\gamma^2}\left(\frac{1}{T_1T}\right)_x = {} & A_{xy}^2\left[J_1\left(\xi_x^{-2}-\varphi_{xy}\right)+J_1\left(\xi_y^{-2}+\varphi_{yx}\right)\right]+A_{xz}^2\left[J_3\left(\xi_x^{-2}-\varphi_{xy}\right)+J_2\left(\xi_y^{-2}+\varphi_{yx}\right)\right]\\
&+A_{yy}^2\left[J_1\left(\xi_y^{-2}-\varphi_{yx}\right)+J_1\left(\xi_x^{-2}+\varphi_{xy}\right)\right]+A_{yz}^2\left[J_2\left(\xi_y^{-2}-\varphi_{yx}\right)+J_3\left(\xi_x^{-2}+\varphi_{xy}\right)\right]\\
&+A_{yz}^2\left[J_2\left(\xi_z^{-2}-\varphi_{zz}\right)+J_3\left(\xi_z^{-2}+\varphi_{zz}\right)\right]+A_{zz}^2\left[J_1\left(\xi_z^{-2}-\varphi_{zz}\right)+J_1\left(\xi_z^{-2}+\varphi_{zz}\right)\right]
\end{aligned} \tag{18}$$

as well as

$$\begin{aligned}
\frac{\Gamma}{8\gamma^2}\left(\frac{1}{T_1T}\right)_y = {} & A_{xx}^2\left[J_1\left(\xi_x^{-2}-\varphi_{xy}\right)+J_1\left(\xi_y^{-2}+\varphi_{yx}\right)\right]+A_{xz}^2\left[J_3\left(\xi_x^{-2}-\varphi_{xy}\right)+J_2\left(\xi_y^{-2}+\varphi_{yx}\right)\right]\\
&+A_{xy}^2\left[J_1\left(\xi_y^{-2}-\varphi_{yx}\right)+J_1\left(\xi_x^{-2}+\varphi_{xy}\right)\right]+A_{yz}^2\left[J_2\left(\xi_y^{-2}-\varphi_{yx}\right)+J_3\left(\xi_x^{-2}+\varphi_{xy}\right)\right]\\
&+A_{xz}^2\left[J_3\left(\xi_z^{-2}-\varphi_{zz}\right)+J_2\left(\xi_z^{-2}+\varphi_{zz}\right)\right]+A_{zz}^2\left[J_1\left(\xi_z^{-2}-\varphi_{zz}\right)+J_1\left(\xi_z^{-2}+\varphi_{zz}\right)\right]
\end{aligned} \tag{19}$$

and

$$\begin{aligned}
\frac{\Gamma}{8\gamma^2}\left(\frac{1}{T_1T}\right)_z = {} & A_{xx}^2\left[J_1\left(\xi_x^{-2}-\varphi_{xy}\right)+J_1\left(\xi_y^{-2}+\varphi_{yx}\right)\right]+A_{xy}^2\left[J_1\left(\xi_x^{-2}-\varphi_{xy}\right)+J_1\left(\xi_y^{-2}+\varphi_{yx}\right)\right]\\
&+A_{yy}^2\left[J_1\left(\xi_y^{-2}-\varphi_{yx}\right)+J_1\left(\xi_x^{-2}+\varphi_{xy}\right)\right]+A_{xy}^2\left[J_1\left(\xi_y^{-2}-\varphi_{yx}\right)+J_1\left(\xi_x^{-2}+\varphi_{xy}\right)\right]\\
&+A_{xz}^2\left[J_3\left(\xi_z^{-2}-\varphi_{zz}\right)+J_2\left(\xi_z^{-2}+\varphi_{zz}\right)\right]+A_{yz}^2\left[J_2\left(\xi_z^{-2}-\varphi_{zz}\right)+J_3\left(\xi_z^{-2}+\varphi_{zz}\right)\right]
\end{aligned} \tag{20}$$

Here, we defined the integrals:

$$\begin{aligned}
J_1(r) &= \int_{-\pi}^{\pi}\int_{-\pi}^{\pi}\frac{dq_xdq_y}{(2\pi)^2}\frac{\cos^2\left(\frac{q_x}{2}\right)\cos^2\left(\frac{q_y}{2}\right)}{\left[r+\left(\cos q_x-\cos q_y+2\right)\right]^2}\equiv\int_{-\pi}^{\pi}\int_{-\pi}^{\pi}\frac{dq_xdq_y}{(2\pi)^2}\frac{\sin^2\left(\frac{q_x}{2}\right)\sin^2\left(\frac{q_y}{2}\right)}{\left[r+\left(\cos q_x-\cos q_y+2\right)\right]^2}\\
J_2(r) &= \int_{-\pi}^{\pi}\int_{-\pi}^{\pi}\frac{dq_xdq_y}{(2\pi)^2}\frac{\cos^2\left(\frac{q_x}{2}\right)\sin^2\left(\frac{q_y}{2}\right)}{\left[r+\left(\cos q_x-\cos q_y+2\right)\right]^2}\\
J_3(r) &= \int_{-\pi}^{\pi}\int_{-\pi}^{\pi}\frac{dq_xdq_y}{(2\pi)^2}\frac{\sin^2\left(\frac{q_x}{2}\right)\cos^2\left(\frac{q_y}{2}\right)}{\left[r+\left(\cos q_x-\cos q_y+2\right)\right]^2}
\end{aligned} \tag{21}$$

In the limit $\xi_i^{-2} \pm \varphi_{\alpha\beta} \ll 1$, we can approximate the integrals by expanding the integrand near $(\pi, 0)$, yielding:

$$\begin{aligned} J_1(r) &\approx \frac{1}{4\pi} \ln\left(\frac{\Lambda_1}{\sqrt{r}}\right) \\ J_2(r) &\approx \frac{1}{8\pi}\left[1 - \frac{r}{2}\ln\left(\frac{\Lambda_2}{\sqrt{r}}\right)\right] \\ J_3(r) &\approx \frac{1}{2\pi r} \end{aligned} \tag{22}$$

where $\Lambda_1 \approx 1.45$ and $\Lambda_2 \approx 3.2$ for $r < 0.5$, according to numerical evaluations of the integrals. Note that, as expected from symmetry considerations, $(T_1T)_x^{-1}(-\epsilon) = (T_1T)_y^{-1}(\epsilon)$ and $(T_1T)_z^{-1}(-\epsilon) = (T_1T)_z^{-1}(\epsilon)$.

FITTING THE SPIN LATTICE RELAXATION RATE DATA

The expressions for $(T_1T)_\alpha^{-1}$ given above depend on six parameters: ξ_x, ξ_y, ξ_z, φ_{xy}, φ_{yx}, and φ_{zz}. We first fit the zero-strain data shown in Fig. 3(b) and 3(d) of the main text assuming all the $\varphi_{\alpha\beta} = 0$, and that $\xi_y = \xi_x$. Because the Landau damping term, Γ, is unknown, one cannot simply extract the $\xi_{x,z}$ directly from the data. However, the ratio of $(T_1T)_x^{-1}/(T_1T)_z^{-1}$ does constrain the data and enable us to fit the data using the temperature-dependent correlation lengths shown in Fig. 4(b) of the main text. The hyperfine coupling constants are given by: $A_{xx} = A_{yy} = 0.66$ T/μ_B, $A_{zz} = 0.47$ T/μ_B, and $A_{xz} = A_{yz} = 0.43$ T/μ_B [20], and we assume the value $A_{xy} = 0.33$ T/μ_B [15].

Using these values for $\xi_{x,z}$ and assuming that $\xi_y = \xi_x$, we then proceed to fit the strain-dependent $(T_1T)^{-1}$ data to the three nematic order parameters, $\varphi_{xy} = \chi_{\text{nem}}^{(xy)}\epsilon$, $\varphi_{yx} = \chi_{\text{nem}}^{(yx)}\epsilon$, and $\varphi_{zz} = \chi_{\text{nem}}^{(zz)}\epsilon$, where the $\chi_{\text{nem}}^{(\alpha\beta)}$ are the static nematic susceptibilities of the three components of the nematic order. These data are shown in Fig. 4 of the main text as a function of temperature.